This is a preprint, the final version is subject to change, of the American Mineralogist (MSA)
Cite as Authors (Year) Title. American Mineralogist, in press.
DOI: https://doi.org/10.2138/am-2018-6437

6437R: **Revision 1** (22.03.2018)

Electron microprobe technique for the determination of iron oxidation state in silicate glasses

Chao Zhang[1], Renat R. Almeev[1,*], Ery C. Hughes[2], Alexander A. Borisov[3], Eric P. Wolff[1], Heidi E. Höfer[4], Roman E. Botcharnikov[5] and Jürgen Koepke[1]

1 Leibniz Universität Hannover, Institut für Mineralogie, Callinstrasse 3, D-30167, Hannover, Germany

2 School of Earth Sciences, University of Bristol, Bristol BS8 1RJ, UK

3 Institute of Geology of Ore Deposits, Petrography, Mineralogy, and Geochemistry, Russian Academy of Sciences, Staromonetny 35, 109017 Moscow, Russia

4 Institut für Geowissenschaften, Mineralogie, Johann Wolfgang Goethe-Universität, Altenhöferallee 1, D-60438 Frankfurt am Main, Germany

5 Institute für Geowissenschaften, Johannes Gutenberg Universität Mainz, J-J-Becher-Weg 21, D-55128 Mainz, Germany

* Corresponding author. Email: r.almeev@mineralogie.uni-hannover.de

ABSTRACT

We present a new calibration for the determination of the iron oxidation state in silicate glasses by electron probe micro-analysis (EPMA) with the "flank method". This method is based on the changes in both intensity and wavelength of the Fe$L\alpha$ and Fe$L\beta$ X-ray emission lines with iron oxidation state. The flank method utilizes the maximum difference for the Fe$L\alpha$ and Fe$L\beta$ spectra observed at the peak flanks between different standard materials, which quantitatively correlates with the Fe^{2+} content. Provided that this correlation is calibrated on reference materials, the $Fe^{2+}/\Sigma Fe$ ratio can be determined for samples with known total Fe content. Two synthetic Fe-rich ferric and ferrous garnet endmembers, i.e. andradite and almandine, were used to identify the Fe$L\alpha$ and Fe$L\beta$ flank method measuring positions that were then applied to the measurement of a variety of silicate glasses with known $Fe^{2+}/\Sigma Fe$ ratio (ranging from 0.2 to 1.0). The measured intensity ratio of Fe$L\beta$ over Fe$L\alpha$ at these flank positions ($L\beta/L\alpha$) is a linear function of the Fe^{2+}content (in wt%). A single linear trend can be established for both garnets and silicate

glasses with 4–18 wt% FeO_T (total iron expressed as FeO). In glasses with up to 18 wt% FeO_T and 15 wt% TiO_2, no systematic compositional (matrix) effects were observed. A possible influence of Ti on the Fe^{2+} determination has only been observed in one high-Ti glass with ~25 wt% TiO_2, a content that is not typical for natural terrestrial silicate melts. The accuracy of the $Fe^{2+}/\Sigma Fe$ determination, which depends on both the Fe^{2+} content determined with the flank method and on the total Fe content, is estimated to be within ±0.1 for silicate glasses with FeO_T >5 wt% and within ±0.3 for silicate glasses with low FeO_T ≤5 wt%. The application of the flank method on silicate glasses requires minimization of the EPMA beam damage which can be successfully achieved by continuous movement of the sample stage under the electron beam during analysis, e.g. with a speed of 2 μm/s.

INTRODUCTION

Fe is the most abundant transition metal in magmatic systems of the Earth. Depending on the redox condition, Fe can be present in different oxidation states (Fe^{3+}, Fe^{2+}, and Fe^0). The oxidation state of Fe in natural silicate glasses is an important parameter that reflects the redox conditions prevailing during magma generation and/or crystallization (e.g. Christie et al., 1986; Bézos and Humler, 2005; Cottrell and Kelley, 2011; Kelley and Cottrell, 2009). It varies as a complex function of oxygen fugacity, temperature, pressure, and melt composition (e.g., Sack et al., 1981; Borisov and Shapkin, 1990; Kress and Carmichael, 1991; Nikolaev et al., 1996; Moretti, 2005; Schuessler et al., 2008; Borisov et al., 2015). Due to the influence of ferrous and ferric Fe on the local structure of silicate melt, the oxidation state of Fe can significantly influence physical and chemical properties of silicate melts (e.g., viscosity, density, heat capacity, degree of polymerization and phase equilibrium, see review by Wilke, 2005).

Both bulk and *in-situ* techniques are available to determine the oxidation state of Fe in geological samples, which is usually expressed as $Fe^{2+}/\Sigma Fe$ or $Fe^{3+}/\Sigma Fe$. The wet-chemistry colorimetric method of Wilson (1960) has been used as the most popular bulk analytical method providing a high accuracy (e.g., Schuessler et al., 2008). For the purpose of non-destructive and/or local high-resolution analysis, several *in-situ* techniques have been developed, such as micro-Mössbauer spectroscopy (McCammon, 1991; Potapkin et al., 2012), X-ray absorption near edge structure (XANES) spectroscopy (Wilke, 2002), electron energy loss spectroscopy (EELS) (van Aken et al., 1998; van Aken and Liebscher, 2002) and micro-Raman spectroscopy (Di Muro et al., 2009). Electron probe micro-analysis (EPMA) has also been utilized to determine the $Fe^{2+}/\Sigma Fe$ ratio in geological samples, such as iron oxides (Höfer et al., 2000), garnets (Höfer and Brey, 2007), olivines (Ejima et al., 2011), amphiboles (Enders et al., 2000; Lamb et al., 2012) and silicate glasses (Fialin et al., 2001; 2004; 2011). Despite methodological challenges observed so far, such as low sensitivity in some analytical protocols and lack of standard materials, the easy access and low costs of EPMA compared to other methods keep it as a promising routine method for measuring the oxidation state of iron in various geological samples including silicate glasses.

In this paper, we present a new analytical technique for measuring the Fe oxidation state of silicate glasses with the EPMA flank method (Höfer and Brey, 2007). Our tests performed on a number of silicate glasses show that the method can provide determination of $Fe^{2+}/\Sigma Fe$ with an accuracy of ±0.1 for glasses containing 5–18 wt% FeO_T, and up to ±0.3 for glasses containing $FeO_T \leq 5$ wt%.

THE FLANK METHOD

The application of EPMA to determine the oxidation state of Fe is based on the peak shift and energy difference of the Fe*L*α and Fe*L*β emission lines for divalent and trivalent iron, which are induced by different electron energies of different bonding associated with Fe^{2+} and Fe^{3+} and their different self-absorption (see details in Fischer, 1965; Tossell et al., 1974; Höfer et al., 1994). Changing from Fe^{2+} to Fe^{3+}, the Fe*L*α and Fe*L*β lines are both shifted to a higher energy, and the intensity of *L*β peak is reduced preferentially to the *L*α peak (Höfer et al., 1994). To date, two quantification techniques have been proposed: the "peak-shift method" and the "flank method".

The *peak-shift method* utilizes the correlation between the peak positions of the Fe*L*α line and $Fe^{3+}/\Sigma Fe$ ratio (Kimura and Akasaka, 1999; Fialin et al., 2001; Fialin et al., 2004; Fialin et al., 2011). The peak-shift method requires accurate peak searches of the Fe*L*α line for all materials under investigation (both standards and unknowns), and may have large uncertainties for samples with low total Fe. This method does not consider the changes in intensity between the Fe*L*α and Fe*L*β emission lines.

The *flank method* exploits both the peak shift and the intensity change of the Fe*L*α and Fe*L*β lines with ferric iron content by measuring the intensities at specific positions on the flanks of Fe*L*α and Fe*L*β peaks, respectively. Therefore, the flank method demonstrates higher sensitivity and better accuracy when compared to the peak-shift method (Höfer et al., 1994; Höfer and Brey, 2007). So far, no application of the EPMA flank method for silicate glasses has been reported in the literature.

For the flank method, the optimal Fe*L*α flank and Fe*L*β flank positions can be determined by the difference spectrum for a pair of materials with similar crystal structure and/or Fe coordination polyhedra but contrasting Fe oxidation states, such as wüstite-hematite (Höfer et al.,

1994; Höfer et al., 2000) and andradite-almandine (**Figure 1; **Höfer, 2003; Höfer and Brey, 2007). The andradite ($Ca^{2+}_3Fe^{3+}_2Si_3O_{12}$) and almandine ($Fe^{2+}_3Al^{3+}_2Si_3O_{12}$) used by Höfer (2003) and Höfer and Brey (2007) are synthetic garnet endmembers containing Fe^{3+} and Fe^{2+}, respectively. As shown by Höfer and Brey (2007), the flank positions determined by this "mineral-difference method" are consistent with self-absorption spectra calculated from X-ray emission spectra at different accelerating voltages. The ratio of intensities measured at the Fe$L\beta$ and Fe$L\alpha$ flank positions, expressed in this paper as $L\beta/L\alpha$, is a function of Fe^{2+} content. After some earlier attempts to correlate $L\beta/L\alpha$ with $Fe^{3+}/\Sigma Fe$ or Fe^{3+} content with the flank method (Höfer et al., 1994; Enders et al., 2000; Höfer, 2002), the unambiguous and accurate quantification of $Fe^{3+}/\Sigma Fe$ in garnet was demonstrated by Höfer and Brey (2007). They also found that for different mineral groups (e.g., garnet, olivine, spinel, wüstite, etc), the slopes of the regression lines of $L\beta/L\alpha$ versus Fe^{2+} content may differ significantly, implying that the correlation between $L\beta/L\alpha$ and Fe^{2+} content might be a function of coordination number of Fe^{2+}. Therefore, to achieve the high precision and accuracy of measured Fe oxidation state as it is now achieved in garnets (Höfer and Brey, 2007), it is necessary to calibrate the flank method for each mineral group and glass, i.e. for each crystal or non-crystal structure. While Fe^{2+} in garnet is 8-fold coordinated, the coordination number of Fe^{2+} in silicate glasses is variable (4, 5 or 6, see Wilke et al., 2007). This difference in coordination between garnet and silicate glass needs to be examined before using garnets as standard materials for determining the Fe oxidation state of silicate glasses. As indicated by our tests (see below), the two garnet references (almandine and andradite) and a number of silicate glasses show a consistent correlation between $L\beta/L\alpha$ and Fe^{2+} content. Therefore, we propose that garnets can be used as standards for measuring the Fe oxidation state of silicate glasses using the EPMA flank method.

SAMPLE SELECTION

Two end-member garnets (Höfer and Brey, 2007) with ferric (andradite, $Ca^{2+}{}_3Fe^{3+}{}_2Si_3O_{12}$) and ferrous (almandine, $Fe^{2+}{}_3Al^{3+}{}_2Si_3O_{12}$) iron were used to calibrate the flank method in this study. Forty-five silicate glasses belonging to five different glass groups were measured (**Table 1**), including twenty-nine Na- and K-free synthetic glasses (Borisov et al., 2004; Borisov, 2007; Borisov et al., 2015), seven synthetic alkali-bearing glasses (ferrobasalts and basaltic andesite), two synthetic hydrous glasses, four re-melted natural glasses (MORB and basanite), and three natural basaltic glass references from the Smithsonian Microbeam Standards collection (USNM 111240/52 VG-2, USNM 113498/1 VG-A99 and USNM 113716, Jarosewich et al., 1980). The synthesized or re-melted glasses were treated experimentally under controlled oxygen fugacity (see **Table 1** for experimental conditions), and these glasses cover a wide range of FeO_T content (4–18 wt%) and $Fe^{2+}/\Sigma Fe$ ratio (0.2–1.0).

WET CHEMISTRY ANALYSIS OF FE OXIDATION STATE

The oxidation state of Fe in all selected experimental glasses has been analyzed using a wet chemistry technique based on the colorimetric method of Wilson (1960) that was modified following the procedure given by Schuessler et al. (2008). The sample powders were first placed in an ammonium vanadate solution, which was then mixed with sulfuric acid. With additional HF, the mixed solution was sealed and kept overnight at room temperature. In this technique Fe^{2+} is oxidized to Fe^{3+} due to the simultaneous reduction of V^{5+} to V^{4+}. Afterwards, the excess HF in the solution was neutralized by adding saturated boric acid solution. The resultant solution was then mixed with quantified ammonium acetate solution, 2:2' bipyridyl solution and distilled water. The pH value in the solution was adjusted to ~5 as buffered by ammonium acetate. The complex of Fe^{2+} with 2:2' bipyridyl shows an intensive absorption band at ~523 nm, which

allows quantification of Fe^{2+} by UV spectrometer. We used a Shimadzu UV-1800 spectrometer on the same solution to measure Fe^{2+} and total Fe before and after adding hydroxylamine hydrochloride solution (this reducing agent forces total Fe as Fe^{2+}). This method ensures that the uncertainty in measured $Fe^{2+}/\Sigma Fe$ is exclusively sourced from the spectrometric measurement but not related to weighing and dilution errors. An in-house standard andesite PU-3 (with known $Fe^{2+}/\Sigma Fe$ =0.39±0.03; Schuessler et al., 2008) and USGS basaltic standard BHVO-1 ($Fe^{2+}/\Sigma Fe$ =0.77±0.03) were measured over all analytical sessions, and the results were identical within the error.

ELECTRON PROBE MICRO-ANALYSIS

Measurements of Fe oxidation state in silicate glasses using the flank method as well as the major element analyses have been performed with a Cameca SX100 electron microprobe equipped with five spectrometers and "PeakSight" operation software at the Institute of Mineralogy, Leibniz Universität Hannover, Germany. All standards and samples were coated with a thin carbon layer with a thickness of ca. 200 Å. The major elements (including total Fe as FeO_T) were measured using calibration standards of synthetic oxides (Al_2O_3, Fe_2O_3, Mn_3O_4, MgO and TiO_2), natural wollastonite (for Si and Ca), orthoclase (for K), jadeiite (for Na) and fluorapatite (for P). The quantifications of all major elements were based on *K*α intensities, and raw data were corrected using the standard PAP procedure (Pouchou and Pichoir, 1991). The accelerating voltage was set at 15 kV for measuring both the major elements and *L*β/*L*α, as recommended by Höfer and Brey (2007). For alkali-free glasses, major elements were measured with a focused 15 nA beam (Borisov et al. 2004; Borisov 2007; Borisov et al. 2015). For alkali-bearing glasses, we used a defocused beam (10 μm diameter) and a lower current (10 nA) to minimize the loss of alkalis during electron bombardment of the sample surface. At least ten

points were measured on fresh surface of each sample (i.e., locations where not previously bombarded) to obtain averages and standard deviations for elemental analyses.

For flank method measurements, we first collected Fe*L*α and Fe*L*β spectra in garnets. The settings of the TAP spectrometer were optimized to measure the Fe*L* lines according to the recipe given by Höfer and Brey (2007). This includes the optimization of the pulse-height analysis (PHA) setting for the Fe*L*α line and the use of the "differential mode" for the X-ray counter. The differential mode was used to diminish high-energy X-ray lines (such as the 9th order of Fe*K*α X-Ray emission line) that are common when using the integral mode (**Figure 1a**). A beam current of 200 nA and 10 µm diameter was used to increase the intensity of the signal, and the sample stage was moved during analysis to diminish beam damage (see below).

As the *first step* of the method, the optimal positions of Fe*L*α and Fe*L*β flanks were determined by collecting Fe*L* X-ray emission spectra of andradite and almandine. **Figure 1b** shows the results indicating that the relative positions and intensities of the Fe*L*α and Fe*L*β peaks are displaced for both Fe^{2+} and Fe^{3+} endmembers. Before subtracting the spectra to obtain the difference spectrum as described in Höfer and Brey (2007), we normalized the spectra to equal total Fe concentration (i.e., spectra intensity divided by mineral total Fe content) to compensate for the difference in bulk Fe contents between andradite and almandine. The resulting difference spectrum demonstrates minima and maxima (**Figure 1c**). The most prominent minimum and maximum have been selected for the Fe*L*β and Fe*L*α flank positions, respectively (vertical lines in **Figure 1c**). The above difference spectra calculation has been measured with a relatively short acquisition time (1000 points, 5 accumulations, 100 ms dwell time). Therefore, the data points of the difference spectrum are scattered resulting in poorly defined flank positions.

This is a preprint, the final version is subject to change, of the American Mineralogist (MSA)
Cite as Authors (Year) Title. American Mineralogist, in press.
DOI: https://doi.org/10.2138/am-2018-6437

In a *second step*, for achieving a better accuracy in defining the flank positions, we performed a flank position adjustment by measuring intensities along a shorter spectral range (from -60 to +60 $10^5 \times \sin\theta$ relative to the approximate flank positions determined in the first step) with a longer acquisition time (120 s). **Figure 2** demonstrates that this procedure allows one to specify a peak position based on a more smoothed spectral pattern compared to the raw spectral scan data. In addition, this second-step adjustment shows that the new re-constrained minimum/maximum positions can be different from the approximate flank positions determined in the first step. As demonstrated by the tests on garnets of Höfer et al. (2000), slight changes in spectrometer position for measuring positions at the flanks would introduce significant variations in measured ratio $L\beta/L\alpha$ between sessions. Due to a variety of potential factors (such as drift of machine conditions, major changes in laboratory conditions, see Höfer and Brey, 2007), the optimal flank positions vary between different analytical sessions, and therefore such flank position adjustment must be performed for each session independently. In addition, to avoid potential problems with oxidation-reduction induced by electron beam bombardment, standards (garnets and glasses) need to be re-polished and carbon-coated before each session (see below).

We acquired the spectral intensities of Fe$L\alpha$ and Fe$L\beta$ at the re-constrained flank positions for both garnet standards and unknown silicate glasses using a beam current of 200 nA and a counting time of 120 s. This high beam current immediately poses the question whether beam damage is significant. Beam damage is well known to be a problem for analyzing alkali-bearing glasses (Morgan VI and London, 1996). For example, in several publications, Fialin and co-authors thoroughly discussed the role of beam-induced Fe oxidation or/and reduction caused by electromigration of alkalis during EPMA analysis (Fialin et al., 2004; Fialin et al., 2001; Fialin and Wagner, 2012). Surprisingly, the same authors reported, “neither oxidation- nor

reduction-induced peak shifts" during measurements of dry and hydrous glasses utilized for the calibration of their peak shift method (Fialin et al., 2011; operating conditions were: 15 kV accelerating potential, 250 nA beam current, 20 μm beam diameter and counting time 240 s). Using static sample stage (conventional analysis, when the same analytical spot is exposed to the beam for the whole acquisition time), we applied the Fialin's et al. (2011) protocol of peak-shift method to our set of experimental glasses, however we failed to observe a robust correlation between the shift of Fe*L*α peak position and Fe oxidation state, which suggests that the calibration of Fialin et al. (2011) should be revised on a more extensive dataset (see Supplementary Figure 1). Thus, our first test measurements clearly demonstrated that beam-induced oxidation/reduction needs to be seriously considered. In this study, to minimize the beam damage, we suggest moving the sample stage with a rate of 2 μm/s during acquisition (see also discussion below). Three independent measurements on different areas (~240*10 μm^2) have been performed for each sample. To check the reproducibility between sessions, analyses of a few samples were replicated during three different analytical sessions (**Table 2**) with a time gap of approximately one month. The ratio of intensities, *L*β/*L*α, measured at the Fe*L*β and Fe*L*α flank positions was then calculated and used for quantifying the Fe oxidation state.

RESULTS

To test the flank method described above, we have measured *L*β/*L*α of the garnet standards and the five silicate glass groups with known Fe oxidation state (**Table 2**). As shown in **Figure 3**, the values of *L*β/*L*α and Fe^{2+} content vary linearly in all sessions. Moreover, all measured glasses lie closely on the trends defined by the garnet standards, indicating that well-characterized garnet endmembers can be used as calibrating standards to quantify the Fe

oxidation state in silicate glasses despite their different coordination of iron cation. The linear relations defined by the garnet standards for the three independent sessions are:

$$Fe^{2+}\,(wt\%) = 34.20\times L\beta/L\alpha - 14.63 \text{ (Session 1)}$$

$$Fe^{2+}\,(wt\%) = 33.47\times L\beta/L\alpha - 13.88 \text{ (Session 2)}$$

$$Fe^{2+}\,(wt\%) = 31.14\times L\beta/L\alpha - 13.66 \text{ (Session 3)}$$

Using these relations and FeO_T concentrations in the glasses, the Fe^{2+} contents and corresponding $Fe^{2+}/\Sigma Fe$ ratios can be calculated (**Table 2**). **Figures 4a**, **4c** and **4e** show that the Fe^{2+} contents determined by the flank method are consistent within error with those determined by wet chemistry in most cases, and the differences are in general less than 1 wt% for all silicate glasses. **Figures 4b**, **4d** and **4f** show that the $Fe^{2+}/\Sigma Fe$ ratios determined by the flank method are consistent within a value of ±0.1 with those determined by wet chemistry for samples with high FeO_T contents (>5 wt%), whereas the ratio difference increase to 0.2–0.3 for samples with lower FeO_T contents. This implies that the error of the $Fe^{2+}/\Sigma Fe$ determined by the flank method is dominantly associated with the intensity measured at the Fe*L* flanks; i.e. the lower the FeO_T content, the lower the accuracy of the analysis.

DISCUSSION

Potential errors of determining $Fe^{2+}/\Sigma Fe$ ratio of glasses using the EPMA flank method can be related to compositional effects, which denotes self-absorption of Fe*L* lines by Fe and variable absorption of Fe*L* lines by other cations (Höfer et al., 1994; Fialin et al., 2001). In order to investigate potential compositional effects, we plotted the difference between Fe^{2+} measured by EPMA and wet chemistry (ΔFe^{2+}) against total Fe content in **Figure 5**. The data do not show any apparent correlation between the measured Fe^{2+} and FeO_T contents, therefore no systematic discrepancy between glasses with contrasting FeO_T contents. This implies that our method of

253 Fe^{2+} determination with the above linear equations is robust and total Fe has little effect on this
254 calibration. As shown by Höfer and Brey (2007), *L*β/*L*α does depend on total Fe, but this effect
255 can be split into the dependence on Fe^{2+} and Fe^{3+} (due to different self-absorption) and can be
256 approximated by a simple linear equation at low total Fe cases (e.g. FeO_T <20 wt%).

257 We explored the potential effect of Ti on the flank method on differentially absorbing
258 Fe*L*α and Fe*L*β within silicate glasses, we explored it within the range of TiO_2 content between 0
259 and 25 wt%. As listed in **Table 2**, for silicate glasses with TiO_2 contents lower than 15 wt%, no
260 systematic correlation is observed between ΔFe^{2+} and TiO_2 content. However, sample DAT32
261 with extremely high TiO_2 (25.09 wt%) demonstrates high ΔFe^{2+} (**Figure 5b**), suggesting that Ti
262 is indeed able to influence the absorption of Fe*L*α and/or Fe*L*β, but only for silicate glasses with
263 very high TiO_2 contents (at least >15 wt%). Although Fialin et al. (2001) emphasized the
264 potential effect of Cr and Ti on Fe *L* line emission and absorption, this problem is perhaps only
265 crucial for Cr- and/or Ti-rich phases (e.g. chromite and ilmenite). The absorption effect of Ti
266 should be extremely weak in silicate glasses with low Ti contents, as demonstrated by the data of
267 Fialin et al. (2004) involving silicate glasses with 0–1.8 wt% TiO_2. This assumption is supported
268 by our results.

269 Potential matrix effects of other elements such as Si, Al, Ca and Mg on the flank method
270 for glasses were not observed in this study, which is consistent with the observations of Höfer
271 and Brey (2007) on garnets. The dataset of silicate glass in this study covers a relatively wide
272 compositional range (**Table 1**), in terms of SiO_2 (40–56 wt%), Al_2O_3 (10–18 wt%), CaO (9–23
273 wt%) and MgO (4–10 wt%), and no systematic influence of these major oxides on *L*β/*L*α in the
274 range of FeO_T (4–18 wt%) was observed. To conclude, our measurements demonstrate that Fe^{2+}
275 in silicate glasses can be calculated from *L*β/*L*α based on the quantitative relation calibrated

against Fe^{2+}-rich and Fe^{3+}-rich garnet endmembers, and there is no significant matrix effect of other cations, except for Ti, if it is present in very high abundances.

Applying the peak-shift method, Fialin et al. (2004) observed both apparent oxidation and reduction trends with accumulated analytical time (at a 15 kV accelerating voltage, 240 nA beam current and 20 μm beam diameter). The observed variation of measured Fe oxidation state with time was attributed by Fialin et al. (2004) to two factors, including (1) Na migration and consequent rearrangement of oxygen atoms between bridging and non-bridging positions in the close vicinity of electron beam bombardment, and (2) buildup of carbon contamination. In this study, we performed additional tests on the anhydrous natural glass reference VG-2 (0.02 wt% H_2O; **Figure 6**) and on basaltic glasses with 0, 2.8 and 5.0 wt% H_2O (**Figure 7**) to illustrate the potential beam damage at 200 nA beam current and associated effects on measurements of $L\beta/L\alpha$, in two contrasting cases with a static sample stage (points) and with a moving stage (horizontal dashed line).

As shown in the left-side panels of **Figure 6**, the values of $L\beta/L\alpha$ measured with a beam diameter from 5 to 20 μm show different behavior with time for the anhydrous basaltic glass VG-2, with the sample stage being static for each measurement. The 5 μm beam induces an overall decrease of $L\beta/L\alpha$ after 250 s, which likely indicates oxidation of the analytical volume due to electron beam bombardment. In contrast, the use of a 10 μm or 20 μm beam tends to increase slightly (or does not modify) the measured ratio of $L\beta/L\alpha$ during the first 250 s. The right-side panels in **Figure 6** show variations of the intensities of Fe$K\alpha$ and Na$K\alpha$ for the beam diameters of 5, 10 and 20 μm, which can provide information on interpreting the variations of $L\beta/L\alpha$. One striking observation is that the loss of the Na$K\alpha$ intensity occurs for all beam sizes, and it is enhanced with decreasing beam size, consistent with previous studies (e.g. Morgan VI

and London, 1996; Fialin et al., 2004). In addition, we show that the Fe*K*α intensity slightly increases when the 5 μm and 10 μm beams were used, and it remains almost constant with the 20 μm beam, demonstrating the tendency of increasing relative Fe content in glass with increase of beam current (probably due to alkali loss and changes of glass density), similar to what has been also shown for Si*K*α and Al*K*α (Morgan VI and London, 1996; Zhang et al., 2016). Provided that *L*β/*L*α is positively correlated with Fe^{2+}content, it seems that severe beam damage (both Na intensity loss and Fe intensity increase) with a small beam size (i.e. 5 μm) tends to oxidize the analyzed glass volume (decreasing $Fe^{2+}/\Sigma Fe$ ratio), whereas weak beam damage (only slight Na intensity loss and no Fe intensity increase) with a large beam size (i.e. 20 μm) tends to reduce (or not modify) the analyzed glass volume (increasing $Fe^{2+}/\Sigma Fe$ ratio).

It is well known that the migration of Na during EPMA (i.e. loss of Na intensity) is much stronger in hydrous glasses than in dry glasses, even if the beam current is as low as 2–5 nA (Morgan VI and London, 1996). On the other hand, water as a chemical component has almost negligible effect on the ferric/ferrous ratio of silicate glasses (Botcharnikov et al., 2005). In this study, we conducted a test of beam damage as a function of time on three glasses with similar major element compositions but different H_2O contents (nominally dry, 2.8 and 5.0 wt% H_2O, **Table 1**). The *L*β/*L*α values and Fe*K*α and Na*K*α intensities have been acquired at 200 nA and 20 μm beam diameter over 500 s with the sample stage being static, which are compared to the values obtained whilst moving the sample stage. The left-side panels of **Figure 7** show the variation of *L*β/*L*α, and the right-side panels show the variation of intensities of Fe*K*α and Na*K*α. With an increase of H_2O content, the loss of Na intensity is dramatically enhanced and Fe*K*α intensity tends to increase. The value of *L*β/*L*α increases slightly during the first 100 s on nominally dry glass N72, consistent with the results obtained on the VG-2 sample measured with

This is a preprint, the final version is subject to change, of the American Mineralogist (MSA)
Cite as Authors (Year) Title. American Mineralogist, in press.
DOI: https://doi.org/10.2138/am-2018-6437

a 20 μm diameter beam (**Figure 6**). In contrast, in H_2O-bearing glasses the *L*β/*L*α value decreases significantly within the same time period, indicating a decrease of Fe^{2+} content in spite of increasing relative total Fe content in the glass as inferred from increasing Fe*K*α intensity. As shown in **Figure 8**, the strong decreases in Na*K*α intensity and *L*β/*L*α are roughly coupled for the hydrous glasses, supporting the hypothesis that the migration of Na during EPMA might promote oxidization of Fe^{2+} converted to Fe^{3+} (Fialin et al., 2004). Therefore, in comparison to dry glasses, the analyzed volume of hydrous glass is much more prone to be oxidized during EPMA as a result of beam damage.

Besides the potential effect of Na-migration on the EPMA measurement of Fe *L*β/*L*α ratio of silicate glasses discussed above, carbon contamination or loss on C-coated sample surface could also play a significant role. Gopon et al. (2013) showed that carbon contamination is a serious problem affecting the measured stabilities of Fe*L*α and Fe*L*β of Fe-Si compounds, especially in cases where a static high-current beam is used. Fialin et al. (2004) found buildup of carbon contamination on silicate glass to be significant when measurements were performed with a 240 nA beam current (20 μm diameter) on the same spot. They suggested that it might have partly resulted in the decrease of measured $Fe^{3+}/\Sigma Fe$ ratio using their peak-shift method, at least for the initial stage of measurement time. Höfer and Brey (2007) made a similar test on an almandine sample with a 60 nA beam scanning an area of 3×5 μm^2, and demonstrated that carbon contamination resulted in decrease in *L*β/*L*α ratio measured by their flank method and in overestimation of $Fe^{3+}/\Sigma Fe$ ratio. Interestingly, the effect of carbon contamination on measuring the Fe oxidation state, observed by Fialin et al. (2004) for silicate glass and by Höfer and Brey (2007) for garnet are contradicting with each other. We tested carbon contamination by measuring the carbon *K*a intensity on the VG-2 glass with static and moving sample stage

This is a preprint, the final version is subject to change, of the American Mineralogist (MSA)
Cite as Authors (Year) Title. American Mineralogist, in press.
DOI: https://doi.org/10.2138/am-2018-6437

respectively. As shown in **Figure 9**, the C*K*a intensity measured on the same spot (i.e., with static sample stage) decreases strongly and continuously with accumulated time up to 400 s, whereas the measurements with moving sample stage demonstrate constant intensity. The observed decrease of C*K*a intensity during beam bombardment is contradicting with Fialin et al. (2004) but consistent with that observed by Gopon et al. (2013). Fialin et al. (2004) observed a continuous increase of C*K*a intensity on a silicate glass for 15 min. However, Gopon et al. (2013) made tests on carbon-coated FeSi compounds with a low-voltage high-current beam (5 kV, 100 nA) and found C*K*a intensity was firstly strongly lost in the initial 400 s but gained later on with accumulated time up to 4000 s. Therefore, the effect of carbon contamination or loss seems to be complicated and probably dependent on a number of factors, such as material composition, beam current, time, etc. In any case, for applying the flank method described in this paper, carbon contamination and loss should be avoided in order to measure glass Fe $L\beta/L\alpha$ ratios, and moving sample stage is demonstrated to be a good approach.

Based on these results, we conclude that, if the EPMA measurements are carried out at the same position for a long time on glasses, the variation of $L\beta/L\alpha$ is a consequence of the combined effects of the changes in both total Fe content and Fe oxidation state of glass, reflecting accumulated material damage induced by electron beam bombardment. Our tests conducted with a static stage demonstrate that the values of $L\beta/L\alpha$ cannot be accurately resolved for dry or hydrous glasses if a high beam current and a long acquisition time are applied. However, our results show that a high accuracy in the determination of the $L\beta/L\alpha$ (and thus $Fe^{2+}/\Sigma Fe$ ratio) can be achieved when analyses are conducted with a continuously moving sample stage (e.g. 2 μm/s) during data acquisition.

IMPLICATIONS

This is a preprint, the final version is subject to change, of the American Mineralogist (MSA)
Cite as Authors (Year) Title. American Mineralogist, in press.
DOI: https://doi.org/10.2138/am-2018-6437

When the beam damage problem is successfully resolved (e.g. by movement of the sample stage in this study), the EPMA flank method provides a promising low-cost and very simple alternative to other local non-destructive techniques, such as XANES, micro-Mössbauer spectroscopy, EELS and micro-Raman spectroscopy (see Introduction for the references). In this study, the accuracy of the $Fe^{2+}/\Sigma Fe$ determination is found to be dependent both on the Fe^{2+} content determined with the flank method and on the total Fe content, and is generally within ±0.1 for silicate glasses with FeO_T >5 wt%.

In petrology, accurately determined $Fe^{2+}/\Sigma Fe$ ratio in natural glasses serves as a proxy of the redox conditions (fO_2) prevailing in magmatic chambers (Christie et al., 1986; Bézos and Humler, 2005; Cottrell and Kelley, 2011). For example, the most recent data obtained by Cottrell and Kelley (2011) by XANES for naturally-quenched pillow-rim glasses suggest that global MORB $Fe^{2+}/\Sigma Fe$ has a value of 0.84±0.01 (1σ) corresponding to the fayalite–magnetite–quartz (FMQ) buffer under conditions of primary magma generation. Assuming 1 wt.% error (2σ) in the determination of Fe^{2+} by the flank EPMA method and an ideal slope of ¼ for the dependence between log (Fe^{3+}/Fe^{2+}) and logfO_2 we provide propagated errors in the determination of fO_2 for the range of $Fe^{2+}/\Sigma Fe$ values typical for natural melts (**Table 3**). Note, however, that additional errors may result from the application of empirical models describing the dependence of ferric/ferrous ratios on temperature, oxygen fugacity and melt composition, and also from differences between real pre-eruptive temperatures of basaltic melts and the temperature of 1200°C typically assumed for ΔFMQ calculations (see discussion in Borisov et al. 2013). As one can see, the translated uncertainties in estimation of the oxygen fugacity for typical MORB ($Fe^{2+}/\Sigma Fe$ ~ 0.85; FeO_T ~ 9 wt%) range within only ±0.12 log units (2σ). This high precision in determination of the $Fe^{2+}/\Sigma Fe$ and in turn fO_2 by the flank EPMA method also provides a new

promising analytical tool for future experimental studies under high pressures, where controlling and logging the redox conditions is usually a challenging task.

ACKNOWLEDGMENTS

We thank Marius Stranghöner and Florian Pohl for the help with wet-chemistry colorimetric method and Julian Feige for sample preparation. We appreciate detailed and insightful comments from John Fournelle and two anonymous reviewers. RA and JK also thank Anette von der Handt and Eric Hellebrandt for support of the project. This study was funded by German Research Foundation (DFG project AL 1189/6-1).

REFERENCES CITED

Almeev, R.R, Holtz, F., Ariskin, A., and Kimura, J.-I. (2013) Storage conditions of Bezymianny Volcano parental magmas: results of phase equilibria experiments at 100 and 700 MPa. Contributions to Mineralogy and Petrology, 166(5), 1389-1414.

Almeev, R.R, Holtz, F., Koepke, J., Parat, F., and Botcharnikov, R.E. (2007) The effect of H_2O on olivine crystallization in MORB: Experimental calibration at 200 MPa. American Mineralogist, 92(4), 670-674.

Bézos, A. and Humler, E. (2005) The $Fe^{3+}/\Sigma Fe$ ratios of MORB glasses and their implications for mantle melting. Geochimica et Cosmochimica Acta 69 (3), 711-725.

Borisov, A. A. and Shapkin, A. I. (1990) A new empirical equation rating Fe^{3+}/Fe^{2+} in magmas to their composition, oxygen fugacity and temperature. Geochemistry International 27, 111–116.

Borisov, A., Behrens, H., and Holtz, F. (2013) The effect of titanium and phosphorus on ferric/ferrous ratio in silicate melts: an experimental study. Contributions to Mineralogy and Petrology, 166(6), 1577-1591.

Borisov, A., Behrens, H., and Holtz, F. (2015) Effects of melt composition on Fe^{3+}/Fe^{2+} in silicate melts: a step to model ferric/ferrous ratio in multicomponent systems. Contributions to Mineralogy and Petrology, 169(2), 1-12.

Borisov, A., Lahaye, Y., and Palme, H. (2004) The effect of TiO_2 on Pd, Ni, and Fe solubilities in silicate melts. American Mineralogist, 89(4), 564-571.

417 Borisov, A.A. (2007) Experimental study of the influence of SiO_2 on the solubility of cobalt and iron in silicate
418 melts. Petrology, 15(6), 523-529.

419 Botcharnikov, R.E., Almeev, R.R., Koepke, J., and Holtz, F. (2008) Phase relations and liquid lines of descent in
420 hydrous ferrobasalt - implications for the Skaergaard Intrusion and Columbia River Flood Basalts. Journal of
421 Petrology, 49(9), 1687-1727.

422 Botcharnikov, R.E., Koepke, J., Holtz, F., McCammon, C., and Wilke, M. (2005) The effect of water activity on the
423 oxidation and structural state of Fe in a ferro-basaltic melt. Geochimica et Cosmochimica Acta, 69(21), 5071-
424 5085.

425 Christie, D. M., Carmichael, I. S. E. and Langmuir, C. H. (1986) Oxidation states of mid-ocean ridge basalt glasses.
426 Earth and Planetary Science Letters 79 (3-4), 397-411.

427 Cottrell, E. and K. A. Kelley (2011) The oxidation state of Fe in MORB glasses and the oxygen fugacity of the
428 upper mantle. Earth and Planetary Science Letters 305(3-4): 270-282.

429 Di Muro, A., Métrich, N., Mercier, M., Giordano, D., Massare, D., and Montagnac, G. (2009) Micro-Raman
430 determination of iron redox state in dry natural glasses: Application to peralkaline rhyolites and basalts.
431 Chemical Geology, 259(1), 78-88.

432 Ejima, T., Akasaka, M., and Ohfuji, H. (2011) Oxidation state of Fe in olivine in a lherzolite xenolith from Oku
433 district, Oki-Dogo Island, Shimane Prefecture, Japan. Journal of Mineralogical and Petrological Sciences,
434 106(5), 246-254.

435 Enders, M., Speer, D., Maresch, W.V., and McCammon, C.A. (2000) Ferric/ferrous iron ratios in sodic amphiboles:
436 Mossbauer analysis, stoichiometry-based model calculations and the high-resolution microanalytical flank
437 method. Contributions to Mineralogy and Petrology, 140(2), 135-147.

438 Fialin, M., Bézos, A., Wagner, C., Magnien, V., and Humler, E. (2004) Quantitative electron microprobe analysis of
439 $Fe^{3+}/\Sigma Fe$: Basic concepts and experimental protocol for glasses. American Mineralogist, 89(4), 654-662.

440 Fialin, M., Wagner, C., Métrich, N., Humler, E., Galoisy, L., and Bézos, A. (2001) $Fe^{3+}/\Sigma Fe$ vs. Fe$L\alpha$ peak energy
441 for minerals and glasses: Recent advances with the electron microprobe. American Mineralogist, 86(4), 456-
442 465.

443 Fialin, M., Wagner, C., and Pascal, M.-L. (2011) Iron speciation using electron microprobe techniques: application
444 to glassy melt pockets within a spinel lherzolite xenolith. Mineralogical Magazine, 75(2), 347-362.

445 Fialin, M. & Wagner, C. (2012) Redox kinetics of iron in alkali silicate glasses exposed to ionizing beams:
446 Examples with the electron microprobe. Journal of Non-Crystalline Solids, 358 (12–13), 1617-1623.

Fischer, D.W. (1965) Changes in the Soft X-Ray L Emission Spectra with Oxidation of the First Series Transition Metals. Journal of Applied Physics, 36(6), 2048-2053.

Fuchs, P., Almeev, R.R., and Klügel, A. (2014) Experimental constraints on the formation of basanites-phonolite series (Cumbre Vieja, La Palma). Goldschmidt Abstracts, 2014 744

Gopon, P., Fournelle, J., Sobol, P.E., and Llovet, X. (2013) Low-voltage electron-probe microanalysis of Fe–Si compounds using soft X-rays. Microscopy and Microanalysis, 19(6), 1698-1708.

Husen, A., Almeev, R.R., and Holtz, F. (2016) The Effect of H_2O and Pressure on Multiple Saturation and Liquid Lines of Descent in Basalt from the Shatsky Rise. Journal of Petrology, 57(2), 309-344.

Höfer, H.E. (2002) Quantification of Fe^{2+}/Fe^{3+} by Electron Microprobe Analysis — New Developments. In P. Gütlich, B.W. Fitzsimmons, R. Rüffer, and H. Spiering, Eds. Mössbauer Spectroscopy: Proceedings of the Fifth Seeheim Workshop, held in Seeheim, Germany, 21–25 May 2002, p. 239-248. Springer Netherlands, Dordrecht.

Höfer, H.E., and Brey, G.P. (2007) The iron oxidation state of garnet by electron microprobe: Its determination with the flank method combined with major-element analysis. American Mineralogist, 92(5-6), 873-885.

Höfer, H.E., Brey, G.P., Schulz-Dobrick, B., and Oberhaensli, R. (1994) The determination of the oxidation state of iron by the electron microprobe. European Journal of Mineralogy, 6(3), 407-418.

Höfer, H.E., Weinbruch, S., McCammon, C.A., and Brey, G.P. (2000) Comparison of two electron probe microanalysis techniques to determine ferric iron in synthetic wüstite samples. European Journal of Mineralogy, 12(1), 63-71.

Jarosewich, E., Nelen, J.A., and Norberg, J.A. (1980) Reference Samples for Electron Microprobe Analysis. Geostandards Newsletter, 4(1), 43-47.

Kelley, K. A. and E. Cottrell (2009) Water and the Oxidation State of Subduction Zone Magmas. Science 325 (5940): 605-607.

Kilinc, A., Carmichael, I.S.E., Rivers, M.L., and Sack, R.O. (1983) The ferric-ferrous ratio of natural silicate liquids equilibrated in air. Contributions to Mineralogy and Petrology, 83(1-2), 136-140.

Kimura, Y., and Akasaka, M. (1999) Estimation of Fe^{2+}/Fe^{3+} and Mn^{2+}/Mn^{3+} ratios by Electron Probe Micro Analyzer. Journal of the Mineralogical Society of Japan, 28, 159-166.

Klügel, A., Galipp, K., Hoernle, K., Hauff, F., and Groom, S. (2017) Geochemical and Volcanological Evolution of La Palma, Canary Islands. Journal of Petrology, 58(6), 1227-1248.

476 Kress, V., and Carmichael, I. (1991) The compressibility of silicate liquids containing Fe_2O_3 and the effect of
477 composition, temperature, oxygen fugacity and pressure on their redox states. Contributions to Mineralogy
478 and Petrology, 108(1), 82-92.

479 Lamb, W.M., Guillemette, R., Popp, R.K., Fritz, S.J., and Chmiel, G.J. (2012) Determination of $Fe^{3+}/\Sigma Fe$ using the
480 electron microprobe: A calibration for amphiboles. American Mineralogist, 97(5-6), 951-961.

481 McCammon, C., Chaskar, V., and Richards, G. (1991) A technique for spatially resolved Mossbauer spectroscopy
482 applied to quenched metallurgical slags. Measurement Science and Technology, 2(7), 657.

483 Moretti, R. (2005) Polymerisation, basicity, oxidation state and their role in ionic modelling of silicate melts. Annals
484 of Geophysics 48 (4-5), 583-608.

485 Morgan VI, G.B., and London, D. (1996) Optimizing the electron microprobe analysis of hydrous alkali
486 aluminosilicate glasses. American Mineralogist, 81, 1176-1185.

487 Nikolaev, G. S., Borisov, A. A. & Ariskin, A. A. (1996) Calculation of the ferric-ferrous ratio in magmatic melts:
488 Testing and additional calibration of empirical equations for various magmatic series. Geochemistry
489 International 34, 641-649.

490 Potapkin, V., Chumakov, A.I., Smirnov, G. V., Celse, J.-P., Rüffer, R., McCammon, C., and Dubrovinsky, L. (2012)
491 The ^{57} Fe Synchrotron Mössbauer Source at the ESRF. Journal of Synchrotron Radiation. 19, 559–569.

492 Pouchou, J.L., and Pichoir, F. (1991) Quantitative analysis of homogeneous or stratified microvolumes applying the
493 model "PAP". In K.F.J. Heinrich, and D.E. Newbury, Eds. Electron probe quantitation, p. 31-75. Plenum
494 Press, New York.

495 Sack, R., Carmichael, I., Rivers, M., and Ghiorso, M. (1981) Ferric-ferrous equilibria in natural silicate liquids at 1
496 bar. Contributions to Mineralogy and petrology, 75(4), 369-376.

497 Savitzky, A., and Golay, M.J.E. (1964) Smoothing and Differentiation of Data by Simplified Least Squares
498 Procedures. Analytical Chemistry, 36(8), 1627-1639.

499 Schuessler, J.A., Botcharnikov, R.E., Behrens, H., Misiti, V., and Freda, C. (2008) Oxidation state of iron in
500 hydrous phono-tephritic melts. American Mineralogist, 93(10), 1493-1504.

501 Shishkina, T., Botcharnikov, R., Holtz, F., Almeev, R. R. & Portnyagin, M. (2010) Solubility of H_2O and CO_2-
502 bearing fluids in tholeiitic basalts at pressures up to 500 MPa. Chemical Geology 277 (1-2), 115-125.

503 Tossell, J., Vaughan, D., and Johnson, K. (1974) Electronic-Structure of Rutile, Wustite, and Hematite from
504 Molecular-Orbital Calculations. American Mineralogist, 59(3-4), 319-334.

van Aken, P., Liebscher, B., and Styrsa, V. (1998) Quantitative determination of iron oxidation states in minerals using Fe L2,3-edge electron energy-loss near-edge structure spectroscopy. Physics and Chemistry of Minerals, 25(5), 323-327.

van Aken, P. A. and Liebscher, B. (2002) Quantification of ferrous/ferric ratios in minerals: new evaluation schemes of Fe L 23 electron energy-loss near-edge spectra. Physics and Chemistry of Minerals 29 (3), 188-200.

Wilke, M., Behrens, H., Burkhard, D.J., and Rossano, S. (2002) The oxidation state of iron in silicic melt at 500 MPa water pressure. Chemical geology, 189(1), 55-67.

Wilke, M. (2005) Fe in magma - An overview. Annals of Geophysics 48 (4-5), 609-617.; Moretti, R. (2005). Polymerisation, basicity, oxidation state and their role in ionic modelling of silicate melts. Annals of Geophysics 48 (4-5), 583-608.

Wilke, M., Farges, F., Partzsch, G.M., Schmidt, C., and Behrens, H. (2007) Speciation of Fe in silicate glasses and melts by in-situ XANES spectroscopy. American Mineralogist, 92(1), 44-56.

Wilson, A. (1960) The micro-determination of ferrous iron in silicate minerals by a volumetric and a colorimetric method. Analyst, 85(1016), 823-827.

Zhang, C., Koepke, J., Wang, L.-X., Wolff, P.E., Wilke, S., Stechern, A., Almeev, R., and Holtz, F. (2016) A Practical Method for Accurate Measurement of Trace Level Fluorine in Mg- and Fe-Bearing Minerals and Glasses Using Electron Probe Microanalysis. Geostandards and Geoanalytical Research, 40(3), 351-363.

FIGURE CAPTIONS

Figure 1. Fe*L* X-ray emission spectra of andradite ($Ca^{2+}_3Fe^{3+}_2Si_3O_{12}$) and almandine ($Fe^{2+}_3Al^{3+}_2Si_3O_{12}$) acquired at 15 kV, beam current 200 nA and beam size 10 μm. (a) Comparison of PHA integral mode and differential mode for Fe*L* X-ray emission spectra of andradite. Note that, for integral mode, there is a small peak between the major Fe*L*α and Fe*L*β peaks, which is the 9th order of the high-energy Fe*K*α X-Ray emission line. (b) Spectra of andradite and almandine acquired in differential mode so the high-energy Fe*K*α X-Ray emission line was diminished. Baseline = 1100 mV, window = 1300 mV, beam current 200 nA, beam size 10 μm, dwell time 0.1 s, accumulation number 5. (c) Difference spectrum (original spectra were acquired with differential mode) between andradite and almandine normalized to equal total Fe content (light in color). Smoothed spectrum (dark in color) is obtained by the Savitzky-Golay method (Savitzky and Golay, 1964). The flank positions of Fe*L*α and Fe*L*β are found at the maximum and minimum of the smoothed difference spectrum (marked by the vertical lines).

Figure 2. Re-constrained flank positions of Fe*L*α (a) and Fe*L*β (b) based on andradite and almandine. The initial flank positions (relative position = 0) are determined by smoothed difference spectra (see Figure 1c). At positions of 0, ±20, ±40 and ±60 relative to the initial flank positions, andradite and almandine were analyzed again with a longer counting time (120 s each, three repeated measurements) to obtain more accurate difference spectra (spots with ±1σ deviation and dashed curve). For comparison, the short-time scan spectra are shown in light grey. See text for details.

Figure 3. Plots of *L*β/*L*α versus Fe^{2+} content for garnets and glasses. Data measured in Session 1 (a), Session 2 (b). and Session 3 (c). Deviation of ±1σ is smaller than symbol size. See details in Table 1.

Figure 4. Comparison of glass Fe^{2+} content and $Fe^{2+}/\Sigma Fe$ ratio determined by EPMA flank method and wet chemistry. Data measured in Session 1 (a-b), Session 2 (c-d). and Session 3 (e-f). The dashed line is ±1 wt% in the left panels and ±0.1 in the right panels.

Figure 5. Difference of Fe^{2+} content (i.e. ΔFe^{2+}) between EPMA flank method and wet chemistry plotted against FeO_T content (see data in Table 1). Data measured in Session 1 (a), Session 2 (b) and Session 3 (c) are plotted separately. Isopleths of induced $\Delta Fe^{2+}/\Sigma Fe$ are also noted in the left panels. The mean standard deviation of calculated ΔFe^{2+} is ca. 0.4 (see inserted error bar). The standard deviation of FeO_T content is smaller than symbol size.

Figure 6. Variation of *L*β/*L*α and count rates of Fe*K*α and Na*K*α as a function of time measured with different beam size for reference glass VG-2. Beam setting is 15 kV and 200 nA for all cases. Dashed line indicates the mean value of *L*β/*L*α measured with moving sample stage, in which case beam damage is minimized.

Figure 7. Variation of *L*β/*L*α and count rates of Fe*K*α and Na*K*α as a function time measured for three glasses (M72, M6 an M11, Shishkina et al., 2010) with different H_2O contents but similar major element composition. Beam current is 200 nA and beam size is 20 μm diameter for all cases. Dashed lines indicate the mean value of *L*β/*L*α measured with moving sample stage, in which case beam damage is minimized.

Figure 8. Plots of *L*β/*L*α versus count rate of Na*K*α for glasses M72, M6 and M11. Beam current is 200 nA and beam size is 20 μm diameter for all cases. The values are for various times during time series measurements, with highest Na signal at the beginning and lowest Na signal at the ending point.

This is a preprint, the final version is subject to change, of the American Mineralogist (MSA)
Cite as Authors (Year) Title. American Mineralogist, in press.
DOI: https://doi.org/10.2138/am-2018-6437

Figure 9. Count rate variations of C*K*α as a function of time measured acquired on VG-2 glass. Beam current and diameter are 200 nA and 20 μm respectively. Note the contrasting variation trends obtained with moving and static sample stage respectively.

Supplementary Figure 1. Experimental glasses used in this study treated by the "peak-shift" calibration from Fialin et al. (2011). Glass and olivine FeLα peak shift positions are scaled to that of hematite standard (measured as a reference to avoid machine drift) and expressed as Δsinθ versus total Fe concentration. Solid line represents the calibration for pure Fe^{2+}, constructed from olivines. Diamonds are experimental glasses used in calibration of Fialin et al. (2011); only the most reduced (filled diamonds) and most oxidized (open diamonds) are shown for clarity. Colored dots are most reduced (green) and oxidized (red) glasses from this study (including some other from Alexander Borisov's collection). Replicate analyses conducted for both oxidized and reduced glasses demonstrate the poor reproducibility utilizing the static beam stage.

TABLE CAPTIONS

Table 1. Major element composition of garnets and silicate glasses (wt%)

Table 2. Fe oxidation state of garnets and silicate glasses

Table 3. Possible errors in fO_2 determination using the flank method for MORB glasses

This is a preprint, the final version is subject to change, of the American Mineralogist (MSA)
Cite as Authors (Year) Title. American Mineralogist, in press.
DOI: https://doi.org/10.2138/am-2018-6437

Figure 1

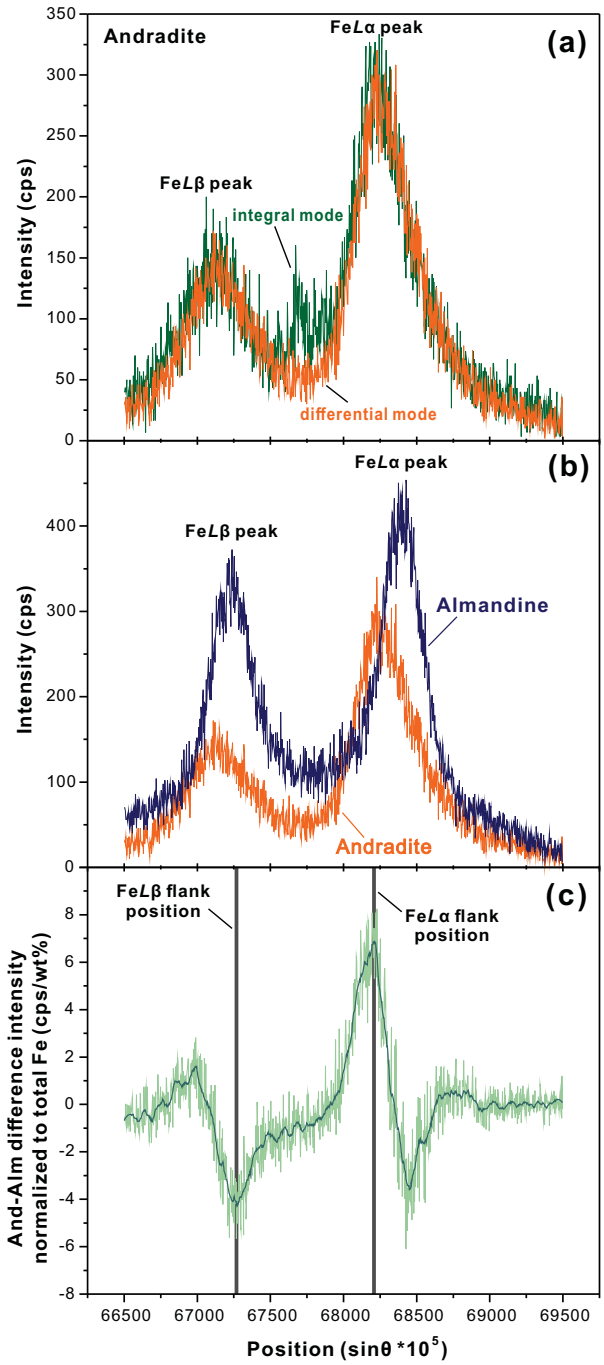

This is a preprint, the final version is subject to change, of the American Mineralogist (MSA)
Cite as Authors (Year) Title. American Mineralogist, in press.
DOI: https://doi.org/10.2138/am-2018-6437

Figure 2

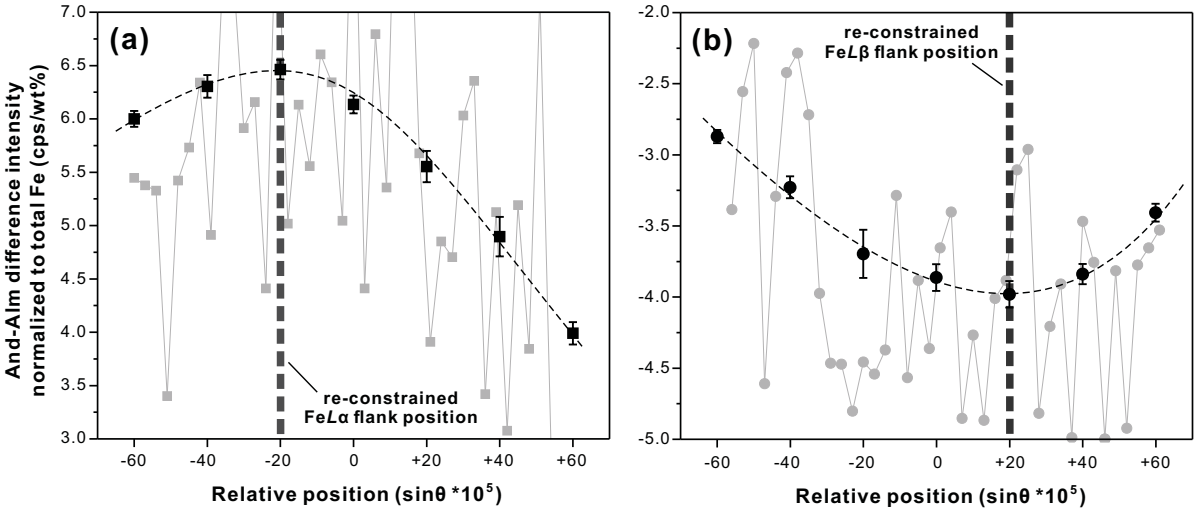

This is a preprint, the final version is subject to change, of the American Mineralogist (MSA)
Cite as Authors (Year) Title. American Mineralogist, in press.
DOI: https://doi.org/10.2138/am-2018-6437

Figure 3

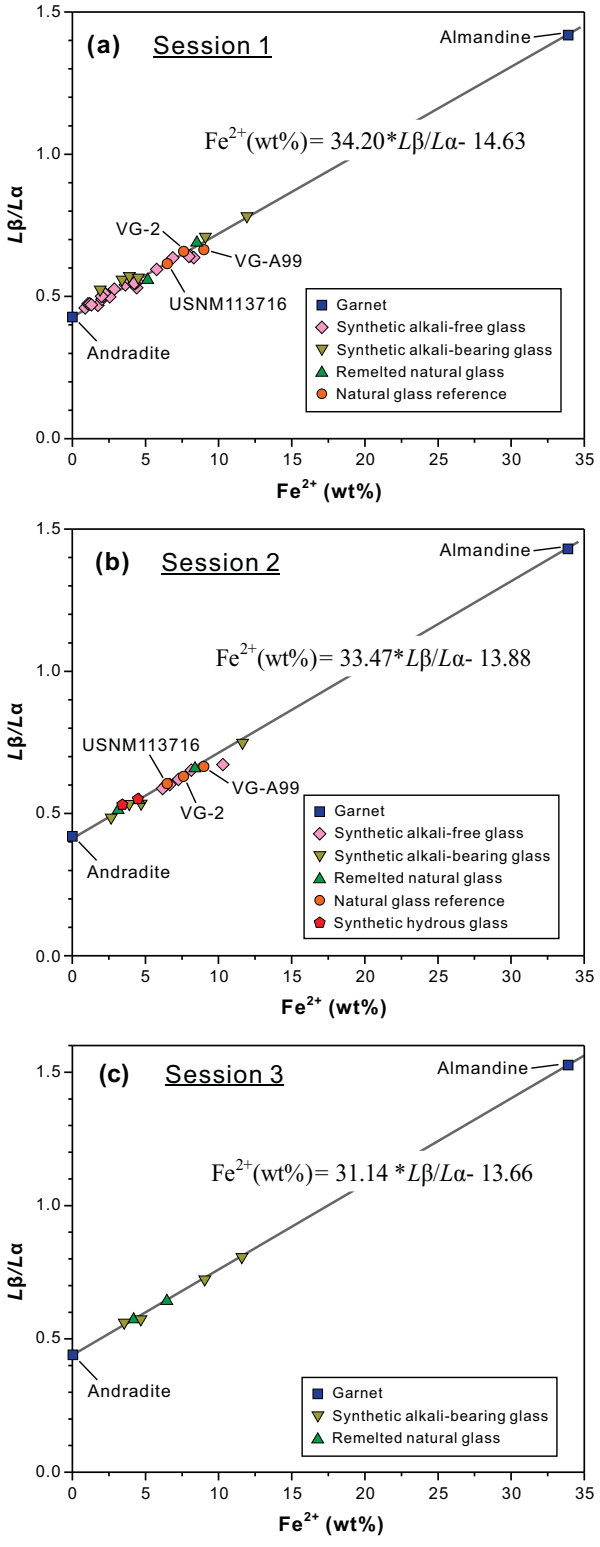

This is a preprint, the final version is subject to change, of the American Mineralogist (MSA)
Cite as Authors (Year) Title. American Mineralogist, in press.
DOI: https://doi.org/10.2138/am-2018-6437

Figure 4

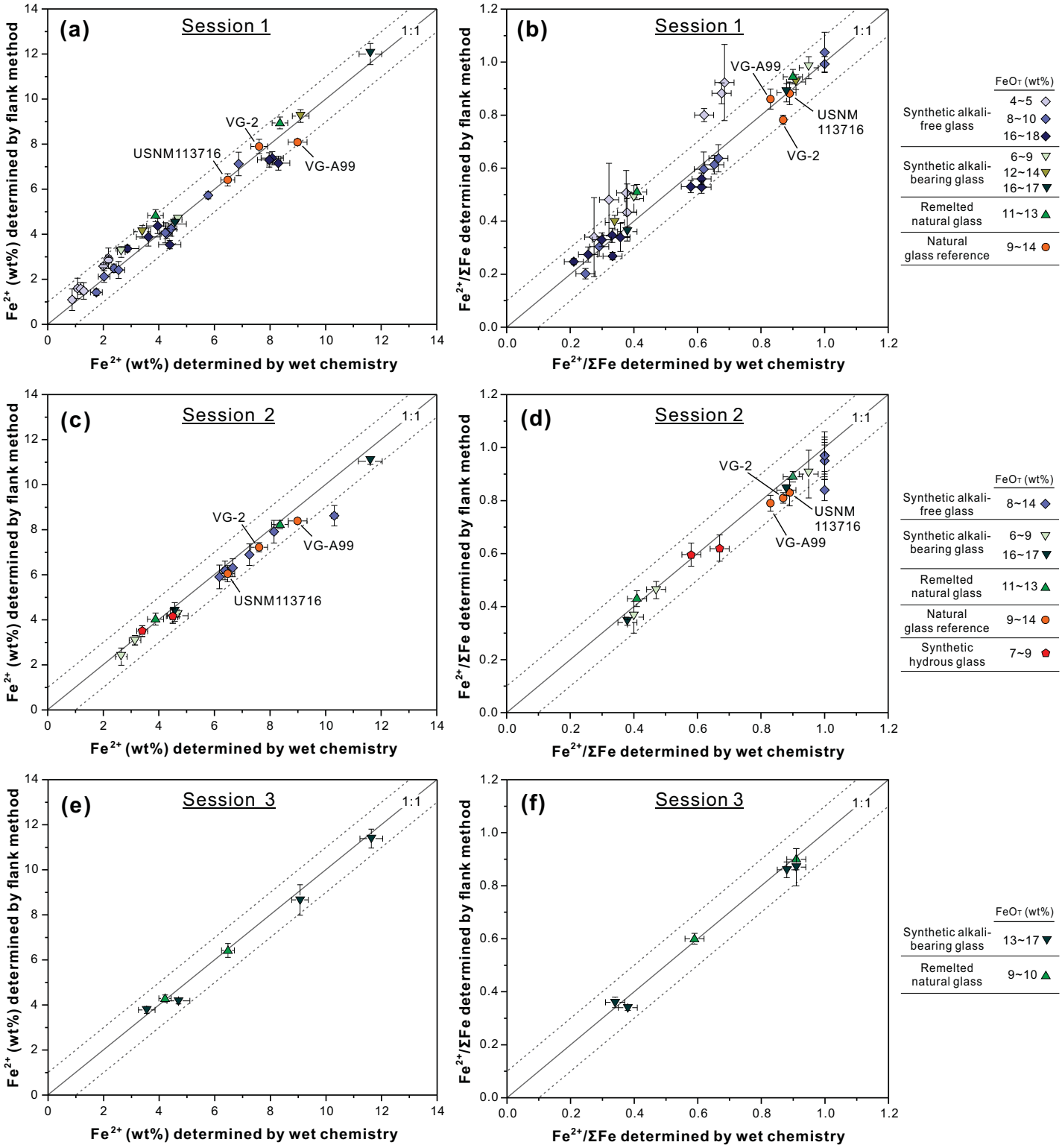

This is a preprint, the final version is subject to change, of the American Mineralogist (MSA)
Cite as Authors (Year) Title. American Mineralogist, in press.
DOI: https://doi.org/10.2138/am-2018-6437

Figure 5

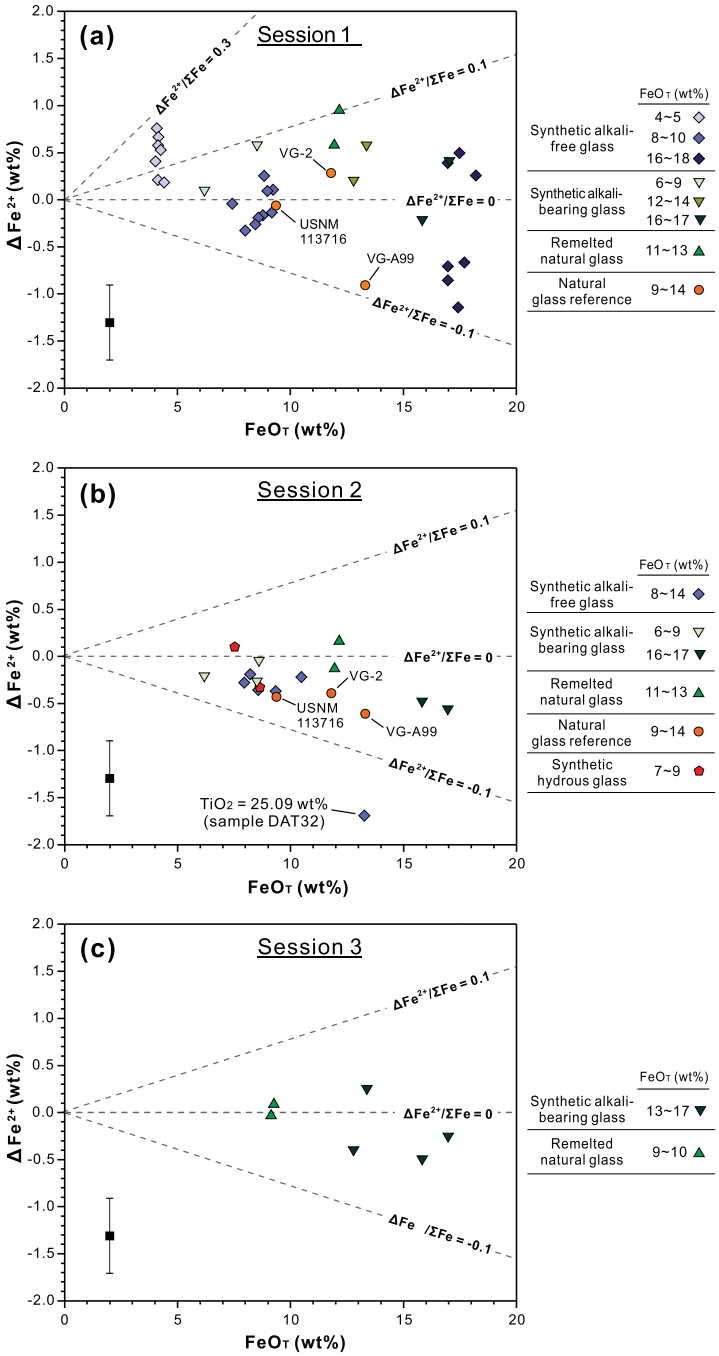

This is a preprint, the final version is subject to change, of the American Mineralogist (MSA)
Cite as Authors (Year) Title. American Mineralogist, in press.
DOI: https://doi.org/10.2138/am-2018-6437

Figure 6

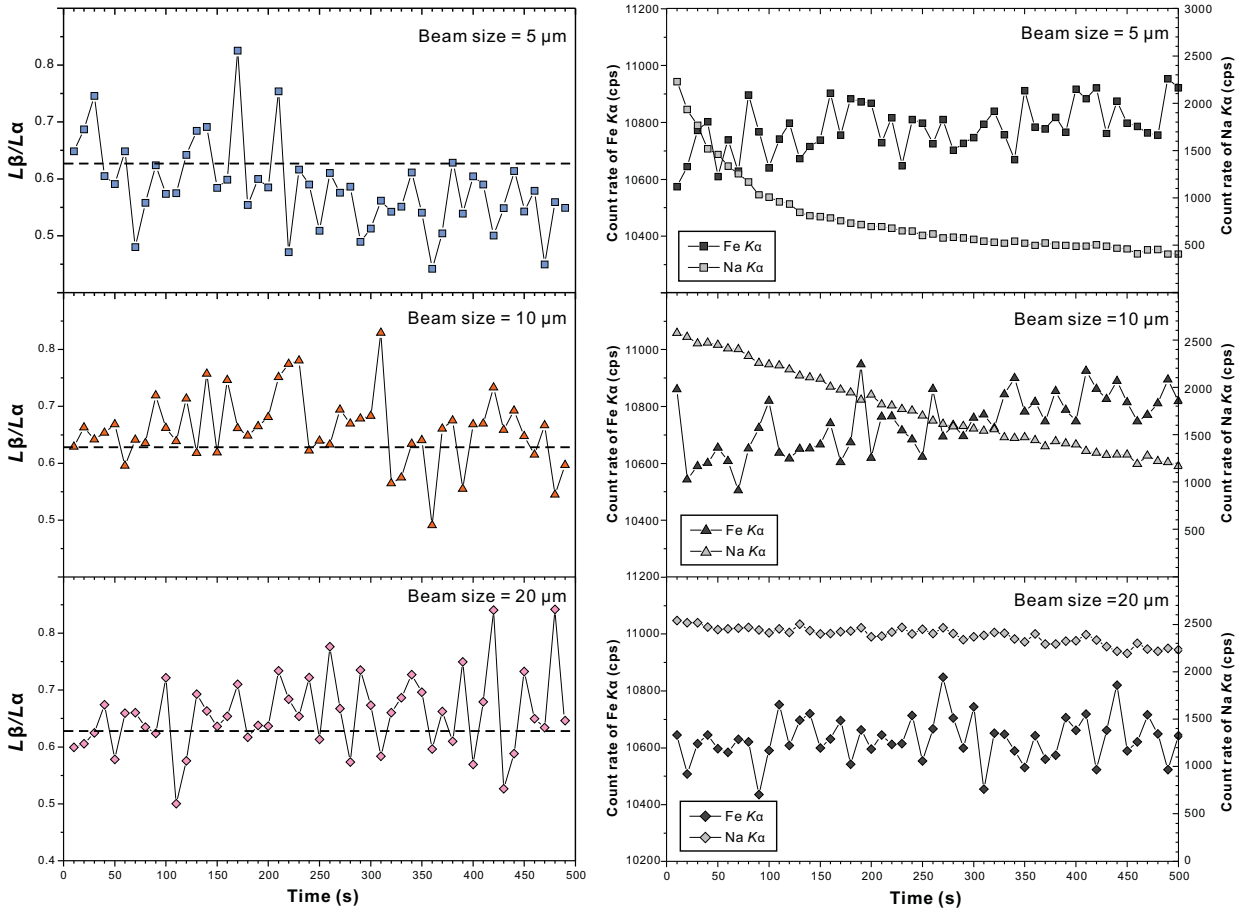

This is a preprint, the final version is subject to change, of the American Mineralogist (MSA)
Cite as Authors (Year) Title. American Mineralogist, in press.
DOI: https://doi.org/10.2138/am-2018-6437

Figure 7

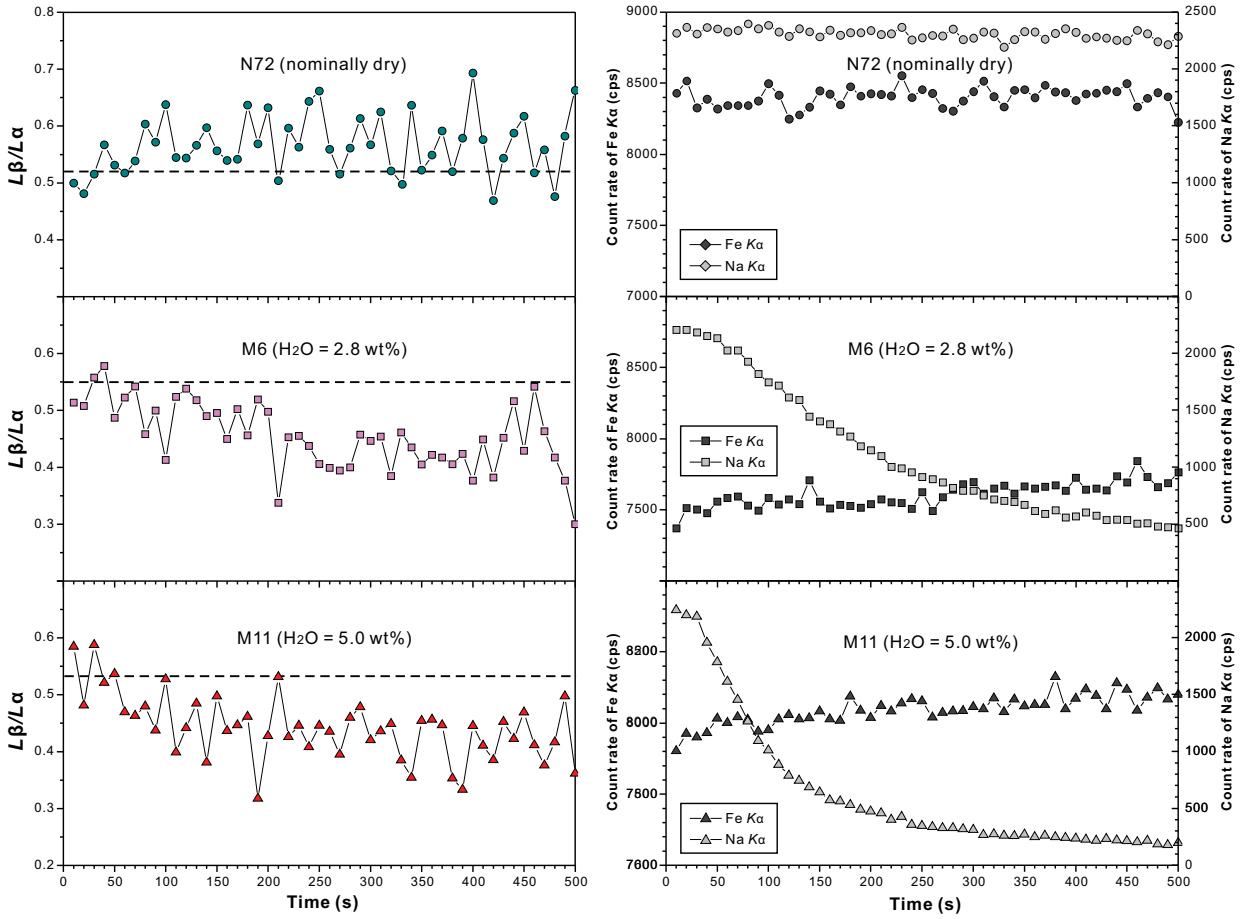

This is a preprint, the final version is subject to change, of the American Mineralogist (MSA)
Cite as Authors (Year) Title. American Mineralogist, in press.
DOI: https://doi.org/10.2138/am-2018-6437

Figure 8

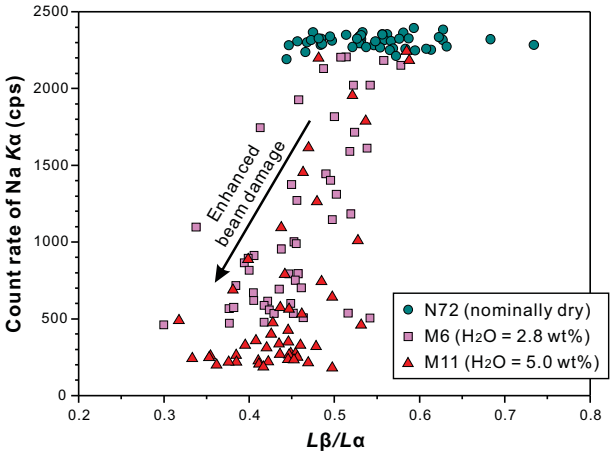

This is a preprint, the final version is subject to change, of the American Mineralogist (MSA)
Cite as Authors (Year) Title. American Mineralogist, in press.
DOI: https://doi.org/10.2138/am-2018-6437

FIGURE 9

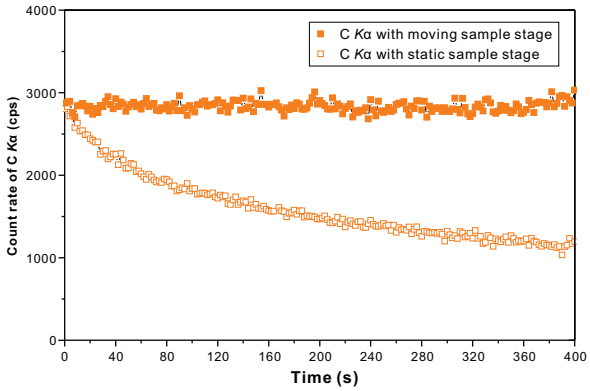

This is a preprint, the final version is subject to change, of the American Mineralogist (MSA)
Cite as Authors (Year) Title. American Mineralogist, in press.
DOI: https://doi.org/10.2138/am-2018-6437

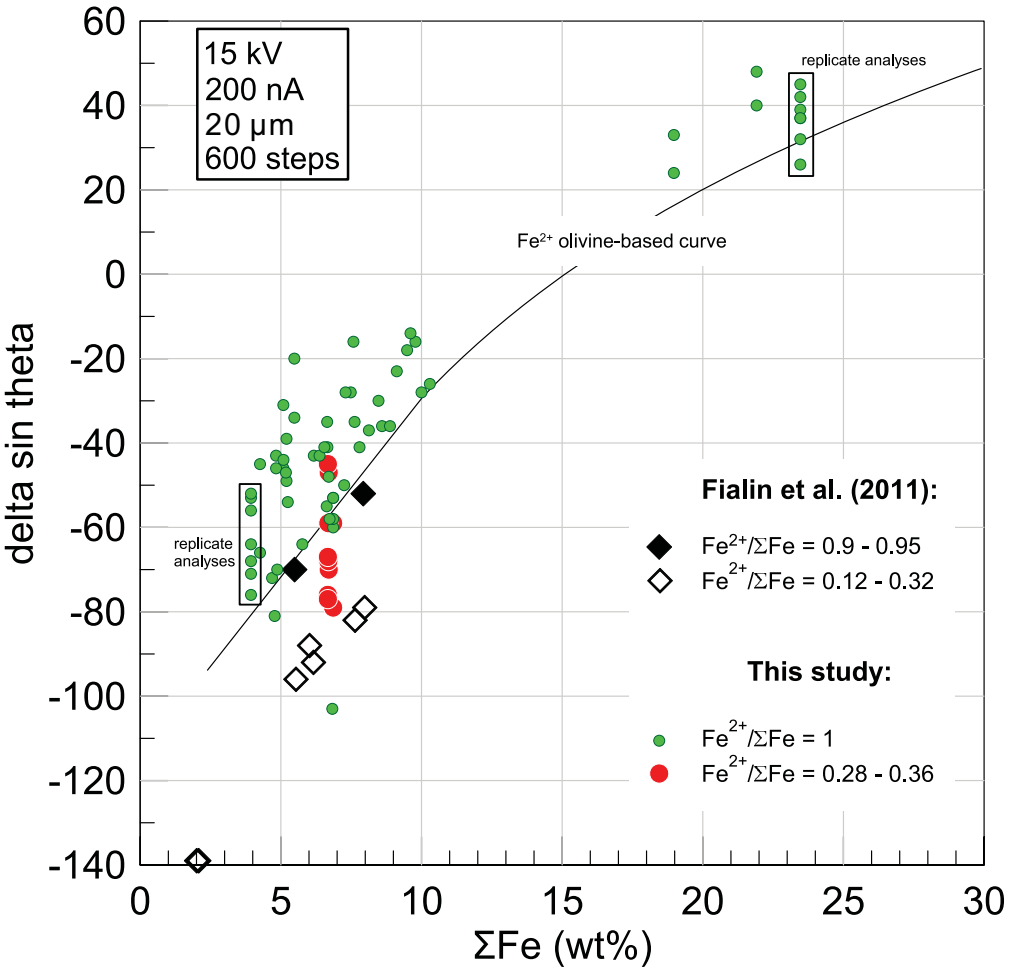

Supplementary Figure 1

Table 1. Major element composition of garnets and silicate glasses (wt%)

Group	Sample No.	SiO_2	TiO_2	Al_2O_3	FeO_T	*std*	MnO	MgO	CaO	Na_2O	K_2O	Total
Garnet	Andradite	34.96	0.02	0.77	27.70	n.d.	0.09	1.01	32.20	0.01	0.03	99.87
	Almandine	35.82	0.00	20.48	43.61	n.d.	0.04	0.53	0.01	0.04	0.00	100.52
Synthetic alkali-free glass	DAFe-6	45.62	b.d.l.	14.57	8.84	*0.08*	b.d.l.	9.54	21.95	b.d.l.	b.d.l.	100.51
	DAFe-7	46.69	b.d.l.	14.68	7.42	*0.07*	b.d.l.	9.72	22.14	b.d.l.	b.d.l.	100.65
	DAF-58	45.62	b.d.l.	14.00	9.07	*0.13*	b.d.l.	8.84	21.25	b.d.l.	b.d.l.	98.78
	DAF5-58	48.05	b.d.l.	15.05	4.14	*0.13*	b.d.l.	9.57	22.68	b.d.l.	b.d.l.	99.49
	DAF20-58	40.31	b.d.l.	12.71	17.48	*0.19*	b.d.l.	8.11	18.94	b.d.l.	b.d.l.	97.55
	DAF-56	45.54	b.d.l.	14.04	8.98	*0.07*	b.d.l.	9.01	21.28	b.d.l.	b.d.l.	98.85
	DAF5-56	48.05	b.d.l.	15.02	4.26	*0.11*	b.d.l.	9.47	22.52	b.d.l.	b.d.l.	99.32
	DAF20-56	40.14	b.d.l.	12.57	18.2	*0.19*	b.d.l.	8.09	18.86	b.d.l.	b.d.l.	97.86
	DAF-57	45.55	b.d.l.	13.97	9.24	*0.12*	b.d.l.	9.00	21.22	b.d.l.	b.d.l.	98.98
	DAF5-57	48.13	b.d.l.	15.10	4.03	*0.09*	b.d.l.	9.72	22.67	b.d.l.	b.d.l.	99.65
	DAF20-57	40.53	b.d.l.	12.75	17.04	*0.24*	b.d.l.	8.12	18.99	b.d.l.	b.d.l.	97.43
	DAF-59	45.51	b.d.l.	14.04	9.17	*0.13*	b.d.l.	9.08	21.27	b.d.l.	b.d.l.	99.07
	DAF5-59	47.97	b.d.l.	14.93	4.4	*0.07*	b.d.l.	9.51	22.47	b.d.l.	b.d.l.	99.28
	DAF20-59	40.69	b.d.l.	12.83	16.97	*0.16*	b.d.l.	8.16	19.06	b.d.l.	b.d.l.	97.71
	DAF-83	45.97	b.d.l.	14.38	8.44	*0.08*	b.d.l.	9.26	21.42	b.d.l.	b.d.l.	99.47
	DAF5-83	48.23	b.d.l.	15.37	4.09	*0.06*	b.d.l.	9.81	22.59	b.d.l.	b.d.l.	100.09
	DAF20-83	41.12	b.d.l.	13.15	16.96	*0.05*	b.d.l.	8.33	19.17	b.d.l.	b.d.l.	98.73
	DAF-84	46.00	b.d.l.	14.39	8.58	*0.05*	b.d.l.	9.23	21.36	b.d.l.	b.d.l.	99.56
	DAF5-84	48.09	b.d.l.	15.29	4.16	*0.05*	b.d.l.	9.74	22.49	b.d.l.	b.d.l.	99.77
	DAF20-84	40.93	b.d.l.	13.15	17.42	*0.08*	b.d.l.	8.35	19.09	b.d.l.	b.d.l.	98.94
	DAF-85	45.71	b.d.l.	15.00	8.78	*0.08*	b.d.l.	9.10	21.02	b.d.l.	b.d.l.	99.61
	DAF5-85	48.15	b.d.l.	15.40	4.15	*0.06*	b.d.l.	9.82	22.53	b.d.l.	b.d.l.	100.05
	DAF20-85	40.77	b.d.l.	13.09	17.7	*0.10*	b.d.l.	8.28	18.96	b.d.l.	b.d.l.	98.80
	DAT	46.91	b.d.l.	14.52	7.95	*0.05*	b.d.l.	9.81	21.76	b.d.l.	b.d.l.	100.96
	DAT3	45.47	2.17	14.26	8.21	*0.07*	b.d.l.	9.67	21.16	b.d.l.	b.d.l.	100.95
	DAT5	44.34	3.93	13.88	8.57	*0.04*	b.d.l.	9.41	20.50	b.d.l.	b.d.l.	100.63
	DAT10	41.73	8.11	12.91	9.34	*0.09*	b.d.l.	8.81	19.13	b.d.l.	b.d.l.	100.02
	DAT17	37.69	14.45	11.80	10.47	*0.12*	b.d.l.	7.99	17.36	b.d.l.	b.d.l.	99.76
	DAT32	31.62	25.09	9.66	13.26	*0.14*	b.d.l.	6.36	14.94	b.d.l.	b.d.l.	100.93
Synthetic alkali-bearing glass	AR39	47.53	2.89	15.05	13.39	0.38	0.04	6.25	11.11	2.45	0.31	99.02
	AR45	48.01	2.77	14.74	12.80	*0.40*	0.01	5.94	10.94	2.55	0.34	98.11
	AR37	51.56	3.72	12.03	15.84	*0.20*	0.35	4.05	9.42	2.75	0.28	99.71
	AR43	50.16	3.48	11.62	16.97	*0.26*	0.30	3.93	8.85	2.90	0.30	98.43
	AR35	53.91	1.01	17.72	8.52	*0.18*	0.20	5.84	8.88	2.80	0.99	99.90
	AR41	55.63	1.04	18.19	6.19	*0.05*	0.16	6.00	9.21	2.59	0.97	100.02
	M72	50.50	0.92	18.40	9.43	*0.20*	0.18	7.05	11.44	2.35	0.23	100.67
Remelted natural glass	AR36	44.73	3.84	13.35	12.16	*0.51*	0.21	8.93	11.82	3.49	1.65	100.37
	AR42	44.30	3.72	13.53	11.95	*0.17*	0.22	8.75	11.95	3.09	1.61	99.07
	AR34	49.07	0.96	15.59	9.16	*0.11*	0.19	9.13	12.22	2.12	0.06	98.50
	AR40	49.60	0.99	16.06	9.13	*0.11*	0.23	9.12	12.17	2.57	0.10	99.96
Natural glass reference	VG-A99	50.94	4.06	12.49	13.3	*0.20*	0.15	5.08	9.30	2.66	0.82	99.18
	VG-2	50.81	1.85	14.06	11.8	*0.20*	0.22	6.71	11.12	2.62	0.19	99.58
	USNM113716	51.52	1.30	15.39	9.36	*0.18*	0.17	8.21	11.31	2.48	0.09	99.95
Natural hydrous glass	M6*	47.68	0.88	17.24	8.53	*0.20*	0.23	6.62	10.72	2.41	0.22	94.33
	M11*	46.44	0.86	16.72	8.19	*0.20*	0.20	6.39	10.46	2.22	0.23	91.70
Starting material for M6 and M11	N72	50.07	0.90	18.36	9.35	*n.d.*	0.17	7.02	11.32	2.45	0.22	100.00

Note: n.d. = not determined. b.d.l. = below detection limit. Standard deviation (1σ) of $Fe^{2+}/\Sigma Fe$ determined by wet chemistry is assumed as 0.03 for all experimental glasses based on estimated uncertainty of the method (see Schuessler et al. 2008). Standard deviation of FeO_T is derived from repeated EPMA measurements (n = 10 to 40). Standard deviation of $Fe^{2+}/\Sigma Fe$ determined by EPMA flank method is calculated according to error propagation.

* M6 and M11 contain 2.8 and 5.0 wt% H_2O, respectively (determined by Karl-Fischer Titration; Shishkina et al., 2010).

All the other glasses are nominally dry.

Synthetic alkali-free glasses:

$DAFe_{ii}$ - series of experimental glasses produced by melting $Di_{58}An_{42}$ eutectic composition in Fe loops below IW buffer conditions (Borisov, 2007);

DAT_{ii} - series of experimental glasses produced by melting $Di_{58}An_{42}$ composition modified with additional TiO_2 in Fe loops below IW buffer (Borisov et al., 2004);

DAF_{ii} - series of experimental glasses produced by melting $Di_{58}An_{42}$ eutectic modified with variable additional Fe_2O_3 in air (Borisov et al. 2015).

Synthetic alkali-bearing glasses:

AR39 and AR45 are oxidized and reduced samples of the ferrobasaltic glass SC1 (Botcharnikov et al., 2008).

AR37 and AR43 are oxidized and reduced samples of the ferrobasaltic glass LS (Botcharnikov and Koepke, unpublished data).

AR35 and AR41 are oxidized and reduced samples of the basaltic andesite glass BezBA (Almeev et al., 2013).

Remelted natural glasses:

AR36 and AR42 are oxidized and reduced samples of the basanite KLA-1-6-22 (Fuchs et al., 2014; Klügel et al., 2017).

AR34 and AR40 are oxidized and reduced samples of the natural MORB glass 140ox (Almeev et al., 2007).

Experimental conditions for synthetic alkali-bearing glasses and remelted natural glasses:

The "oxidized" AR34 – AR39 glasses have been produced in a 1 atm furnace at 1600 °C, in air using Pt crucibles.

The "reduced" AR40 – AR45 glasses have been produced in internally heated pressure vessel at 1250 °C, 200 MPa under intrinsic conditions in Pt-lined graphite capsules (see details in Husen et al. 2016).

The M6 and M11 glasses are H_2O-saturated glasses have been produced in internally heated pressure vessel at 1250 °C, 100 and 200 MPa respectively, under intrinsic conditions in $Au_{80}Pd_{20}$ capsules (see details in Shishkina et al. 2010). Starting glass N72 was produced by re-melting of the island arc-tholeiitic basalt at 1atm furnace at 1600 °C, in air using Pt crucible.

This is a preprint, the final version is subject to change, of the American Mineralogist (MSA)
Cite as Authors (Year) Title. American Mineralogist, in press.
DOI: https://doi.org/10.2138/am-2018-6437

Table 2. Fe oxidation state of garnets and silicate glasses

Sample No.	Total Fe		Wet chemistry				EMPA flank method							Difference between EPMA and wet chemistry	
	FeO_T	*std*	$Fe^{2+}/\Sigma Fe$	*std*	Fe^{2+} (wt%)	*std*	Session	*Lβ/Lα*	*std*	Fe^{2+} (wt%)	*std*	$Fe^{2+}/\Sigma Fe$	*std*	ΔFe^{2+} (wt%)	$\Delta Fe^{2+}/\Sigma Fe$
Garnets															
Andradite	27.70	n.d.	0.00	n.d.	0.00	n.d.	1	0.428	*0.003*	-	-	-	-	-	-
							2	0.415	*0.003*	-	-	-	-	-	-
							3	0.439	*0.004*					-	-
Almandine	43.61	n.d.	1.00	n.d.	33.90	n.d.	1	1.419	*0.023*	-	-	-	-	-	-
							2	1.428	*0.026*	-	-	-	-	-	-
							3	1.527	*0.024*					-	-
Synthetic alkali-free glass															
DAFe-6	8.84	*0.08*	1.00*	n.d.	6.87	*0.06*	1	0.636	*0.015*	7.12	*0.52*	1.04	*0.08*	0.25	0.04
DAFe-7	7.42	*0.07*	1.00*	n.d.	5.77	*0.05*	1	0.595	*0.005*	5.73	*0.16*	0.99	*0.03*	-0.04	-0.01
DAF-58	9.07	*0.13*	0.25	*0.03*	1.76	*0.21*	1	0.469	*0.004*	1.42	*0.14*	0.20	*0.02*	-0.34	-0.05
DAF5-58	4.14	*0.13*	0.28	*0.03*	0.90	*0.10*	1	0.460	*0.014*	1.09	*0.48*	0.34	*0.15*	0.19	0.06
DAF20-58	17.48	*0.19*	0.21	*0.03*	2.85	*0.41*	1	0.526	*0.004*	3.36	*0.14*	0.25	*0.01*	0.51	0.04
DAF-56	8.98	*0.07*	0.29	*0.03*	2.02	*0.21*	1	0.490	*0.007*	2.12	*0.26*	0.30	*0.04*	0.10	0.01
DAF5-56	4.26	*0.11*	0.32	*0.03*	1.06	*0.10*	1	0.474	*0.013*	1.59	*0.45*	0.48	*0.14*	0.53	0.16
DAF20-56	18.2	*0.19*	0.26	*0.03*	3.68	*0.43*	1	0.541	*0.012*	3.88	*0.40*	0.27	*0.03*	0.20	0.01
DAF-57	9.24	*0.12*	0.33	*0.03*	2.37	*0.22*	1	0.500	*0.006*	2.49	*0.19*	0.35	*0.03*	0.12	0.02
DAF5-57	4.03	*0.09*	0.38	*0.03*	1.19	*0.10*	1	0.474	*0.008*	1.59	*0.26*	0.51	*0.08*	0.40	0.13
DAF20-57	17.04	*0.24*	0.30	*0.03*	3.97	*0.40*	1	0.555	*0.010*	4.37	*0.34*	0.33	*0.03*	0.40	0.03
DAF-59	9.17	*0.13*	0.36	*0.03*	2.57	*0.22*	1	0.498	*0.011*	2.42	*0.38*	0.34	*0.05*	-0.15	-0.02
DAF5-59	4.4	*0.07*	0.38	*0.03*	1.30	*0.10*	1	0.471	*0.011*	1.48	*0.37*	0.43	*0.11*	0.18	0.05
DAF20-59	16.97	*0.16*	0.33	*0.03*	4.35	*0.40*	1	0.531	*0.005*	3.54	*0.18*	0.27	*0.01*	-0.81	-0.06
DAF-83	8.44	*0.08*	0.65	*0.03*	4.26	*0.20*	1	0.545	*0.007*	4.02	*0.22*	0.61	*0.03*	-0.24	-0.04
DAF5-83	4.09	*0.06*	0.69	*0.03*	2.19	*0.10*	1	0.514	*0.013*	2.94	*0.45*	0.92	*0.14*	0.75	0.23
DAF20-83	16.96	*0.05*	0.61	*0.03*	8.04	*0.40*	1	0.643	*0.008*	7.38	*0.29*	0.56	*0.02*	-0.66	-0.05
DAF-84	8.58	*0.05*	0.67	*0.03*	4.47	*0.20*	1	0.552	*0.010*	4.25	*0.34*	0.64	*0.05*	-0.22	-0.03
DAF5-84	4.16	*0.05*	0.68	*0.03*	2.20	*0.10*	1	0.511	*0.004*	2.85	*0.12*	0.88	*0.04*	0.65	0.20
DAF20-84	17.42	*0.08*	0.61	*0.03*	8.26	*0.41*	1	0.637	*0.009*	7.16	*0.31*	0.53	*0.02*	-1.10	-0.08
DAF-85	8.78	*0.08*	0.62	*0.03*	4.23	*0.21*	1	0.547	*0.013*	4.07	*0.45*	0.60	*0.07*	-0.16	-0.02
DAF5-85	4.15	*0.06*	0.62	*0.03*	2.00	*0.10*	1	0.503	*0.002*	2.58	*0.07*	0.80	*0.02*	0.58	0.18
DAF20-85	17.7	*0.10*	0.58	*0.03*	7.98	*0.42*	1	0.641	*0.009*	7.30	*0.32*	0.53	*0.02*	-0.68	-0.05
DAT	7.95	*0.05*	1.00*	n.d.	6.18	*0.04*	2	0.591	*0.016*	5.90	*0.53*	0.96	*0.09*	-0.28	-0.04
DAT3	8.21	*0.07*	1.00*	n.d.	6.38	*0.05*	2	0.600	*0.012*	6.19	*0.42*	0.97	*0.07*	-0.19	-0.03
DAT5	8.57	*0.04*	1.00*	n.d.	6.66	*0.03*	2	0.603	*0.012*	6.31	*0.40*	0.95	*0.06*	-0.35	-0.05
DAT10	9.34	*0.09*	1.00*	n.d.	7.26	*0.07*	2	0.621	*0.014*	6.89	*0.48*	0.95	*0.07*	-0.37	-0.05
DAT17	10.47	*0.12*	1.00*	n.d.	8.14	*0.09*	2	0.651	*0.015*	7.91	*0.50*	0.97	*0.06*	-0.23	-0.03
DAT32	13.26	*0.14*	1.00*	n.d.	10.31	*0.11*	2	0.672	*0.014*	8.62	*0.45*	0.84	*0.04*	-1.69	-0.16
Synthetic alkali-bearing glass															
AR39	13.39	0.38	0.34	*0.03*	3.54	*0.33*	1	0.548	0.008	4.11	0.27	0.39	0.03	0.57	0.05
							3	0.560	0.005	3.79	0.15	0.36	0.02	0.25	0.02
AR45	12.80	*0.40*	0.91	*0.03*	9.05	*0.41*	1	0.698	*0.008*	9.25	*0.28*	0.93	*0.04*	0.20	0.02
							3	0.717	*0.022*	8.67	*0.67*	0.87	*0.07*	-0.38	-0.04
AR37	15.84	*0.20*	0.38	*0.03*	4.68	*0.37*	1	0.558	*0.008*	4.46	*0.26*	0.36	*0.02*	-0.22	-0.02
							2	0.540	*0.002*	4.19	*0.06*	0.31	*0.00*	-0.49	-0.07
							3	0.573	*0.004*	4.18	*0.13*	0.34	*0.01*	-0.50	-0.04
AR43	16.97	*0.26*	0.88	*0.03*	11.61	*0.43*	1	0.779	*0.014*	12.00	*0.47*	0.91	*0.01*	0.39	0.03
							2	0.745	*0.004*	11.04	*0.14*	0.81	*0.01*	-0.57	-0.07
							3	0.804	*0.014*	11.38	*0.42*	0.86	*0.03*	-0.23	-0.02
AR35	8.52	*0.18*	0.40	*0.03*	2.65	*0.21*	1	0.522	*0.007*	3.21	*0.24*	0.48	*0.04*	0.56	0.08
							2	0.486	*0.012*	2.11	*0.16*	0.44	*0.03*	-0.54	0.04
AR41	6.19	*0.05*	0.95	*0.03*	4.57	*0.15*	1	0.564	*0.006*	4.65	*0.20*	0.97	*0.04*	0.08	0.02
							2	0.545	*0.012*	4.35	*0.42*	0.92	*0.09*	-0.22	-0.03
M72	9.43	*0.20*	0.47	*0.03*	3.44	*0.23*	2	0.518	*0.006*	3.09	*0.21*	0.46	*0.03*	-0.35	-0.01
Remelted natural glass															
AR36	12.16	*0.51*	0.41	*0.03*	3.88	*0.33*	1	0.569	*0.008*	4.83	*0.28*	0.51	*0.03*	0.95	0.10
							2	0.535	*0.008*	4.03	*0.27*	0.43	*0.03*	0.15	0.02
AR42	11.95	*0.17*	0.90	*0.03*	8.36	*0.30*	1	0.689	*0.008*	8.94	*0.26*	0.96	*0.03*	0.58	0.06
							2	0.661	*0.006*	8.23	*0.19*	0.87	*0.02*	-0.13	-0.03
AR34	9.16	*0.11*	0.59	*0.03*	4.20	*0.22*	3	0.577	*0.005*	4.29	*0.16*	0.60	*0.02*	0.09	0.01

This is a preprint, the final version is subject to change, of the American Mineralogist (MSA)
Cite as Authors (Year) Title. American Mineralogist, in press.
DOI: https://doi.org/10.2138/am-2018-6437

AR40	9.13	*0.11*	0.91	*0.03*	6.46	*0.23*	3	0.645	*0.010*	6.42	*0.31*	0.90	*0.04*	-0.04	-0.01
Natural glass reference															
VG-A99	13.3	*0.20*	0.87**	n.d.	8.99	*0.14*	1	0.664	*0.004*	8.09	*0.13*	0.78	*0.01*	-0.90	-0.09
							2	0.665	*0.004*	8.39	*0.12*	0.81	*0.02*	-0.60	-0.06
VG-2	11.8	*0.20*	0.83**	n.d.	7.61	*0.13*	1	0.659	*0.009*	7.90	*0.32*	0.86	*0.03*	0.29	0.03
							2	0.628	*0.006*	7.22	*0.20*	0.79	*0.02*	-0.39	-0.04
USNM-113716	9.36	*0.18*	0.89**	n.d.	6.48	*0.12*	1	0.615	*0.008*	6.41	*0.27*	0.88	*0.04*	-0.07	-0.01
							2	0605	*0.004*	6.05	*0.36*	0.83	*0.05*	-0.43	-0.06
Synthetic hydrous glass															
M6	8.53	*0.20*	0.67	*0.03*	4.44	*0.22*	2	0.550	*0.009*	4.17	*0.32*	0.62	*0.05*	-0.27	-0.05
M11	8.19	*0.20*	0.58	*0.03*	3.69	*0.21*	2	0.530	*0.007*	3.50	*0.24*	0.60	*0.04*	-0.19	0.02

* Assumed value. The synthetic glasses have been produced in experiments with a Fe-loop, below iron-wüstite buffer conditions (Borisov et al. 2004; Borisov 2007).

** Ratio calculated based on FeO and Fe_2O_3 contents provided in Jarosewich et al. (1980).

This is a preprint, the final version is subject to change, of the American Mineralogist (MSA)
Cite as Authors (Year) Title. American Mineralogist, in press.
DOI: https://doi.org/10.2138/am-2018-6437

Table 3. Possible errors in fO_2 determination using the flank method for MORB glasses

$Fe^{2+}/\Sigma Fe$	FeO_T = 10 wt%		FeO_T = 9 wt%		FeO_T = 8 wt%	
	$\Delta Fe^{2+}/\Sigma Fe$*	$\Delta \log fO_2$**	$\Delta Fe^{2+}/\Sigma Fe$	$\Delta \log fO_2$	$\Delta Fe^{2+}/\Sigma Fe$	$\Delta \log fO_2$
0.95	0.13	0.30	0.14	0.33	0.16	0.37
0.90	0.13	0.16	0.14	0.17	0.16	0.19
0.85	0.13	0.11	0.14	0.12	0.16	0.14
0.80	0.13	0.09	0.14	0.10	0.16	0.11
0.75	0.13	0.07	0.14	0.08	0.16	0.07

* assumed ΔFe^{2+} = 1 wt% (2σ, flank method, EPMA) and $\Delta \Sigma Fe$ = 1 wt% (EPMA);

** assumed ideal slope of 0.25 for $\log(Fe^{3+}/Fe^{2+})$ versus $\log fO_2$.